



# Modulating polarization rotation to stimulate the high piezocatalytic activity of (K, Na)NbO<sub>3</sub> lead-free piezoelectric materials

Xi-xi Sun<sup>a</sup>, Ruichen Li<sup>a</sup>, Zhiwei Yang<sup>c</sup>, Nan Zhang<sup>a</sup>, Chao Wu<sup>a</sup>, Junhua Li<sup>a</sup>, Yulin Chen<sup>a</sup>, Qiang Chen<sup>a</sup>, Jing Zhang<sup>c</sup>, Hongjian Yan<sup>b</sup>, Xiang Lv<sup>a,\*</sup>, Jiagang Wu<sup>a,\*</sup>

<sup>a</sup> Department of Materials Science, Sichuan University, Chengdu 610065, China

<sup>b</sup> College of Chemistry, Sichuan University, Chengdu 610065, China

<sup>c</sup> College of Architecture & Environment, Sichuan University, Chengdu 610065, China

## ARTICLE INFO

### Keywords:

Lead-free  
Potassium sodium niobate  
Polarization rotation  
Piezoelectric response  
Piezocatalytic activities

## ABSTRACT

The strategy of modulating polarization rotation of potassium sodium-niobate ((K<sub>0.5</sub>Na<sub>0.5</sub>)NbO<sub>3</sub>, KNN) lead-free piezoelectric materials was reported to boost piezoelectric properties and resultant piezocatalytic activities. The effectiveness of modulating polarization rotation was proved by degrading Rhodamine B (RhB) using three KNN-based samples with different phase structures (i.e., orthorhombic (O) phase, orthorhombic-tetragonal (O-T) coexistence phase, and rhombohedral-orthorhombic-tetragonal (R-O-T) coexistence phase). Poled samples with the R-O-T coexistence phase show a reaction rate constant of 0.091 min<sup>-1</sup> owing to the easiest polarization rotation, 2.12 times more than that of poled O-phase featured samples with the most difficult polarization rotation. Enhanced piezocatalytic activities primarily originate from the easier polarization rotation and improved carrier concentration, accompanied by the trace of the mechano-charge generation. Therefore, modulating polarization rotation effectively boosts piezocatalysis of KNN-based materials, promising for harnessing natural energy and disease treatment.

## 1. Introduction

As the world energy crisis intensifies, renewable energy, such as solar, wind, and tide, needs to be used more effectively [1–4]. Because of the ability to interconvert mechanical energy and electrical energy directly, the piezoelectric effect has gained popularity and has been used for energy harvesting and conversion [5–13]. In particular, applying periodic ultrasonic waves to piezoelectric materials generates stable and continuous free charges that are conducive to water splitting, degradation dyes, etc [2,4,14–18]. In addition, compared with light, ultrasound has the advantage of stronger penetrating power and is harmless to humans, promising for biomedical applications [19–22]. Thus, applying ultrasound-induced piezocatalysis to disease treatment has also become a research hotspot in recent years [19–22].

In this context, piezoelectric materials, including zinc oxide (ZnO), bismuth-based materials, and molybdenum sulfide (MoS<sub>2</sub>), have been investigated for piezocatalysis [2–4,18,23,24]. Although their piezocatalytic activities have been improved by various methods [4,25,26], the relatively inferior piezoelectric properties limited further enhancement

of the piezocatalytic activities, especially compared with perovskite-structured materials [5,6,27–31]. Therefore, the researchers have turned their eyes to perovskite-structured piezoelectric materials for piezocatalysis studies. At present, these materials mainly include lead-based (e.g., Pb<sub>0.5</sub>Zr<sub>0.5</sub>TiO<sub>3</sub>-based (PZT)) and lead-free ones (e.g., BaTiO<sub>3</sub>-based (BT), BiFeO<sub>3</sub>-based (BFO), Bi<sub>0.5</sub>Na<sub>0.5</sub>TiO<sub>3</sub>-based (BNT) and K<sub>0.5</sub>Na<sub>0.5</sub>NbO<sub>3</sub>-based (KNN)), among which lead-based ones possess highest piezoelectric properties [6,29,32,33]. However, the high content of toxic Pb (~60%) in these lead-based materials contradicts sustainable development and environmental protection. Thus, lead-free piezoelectric materials are in urgent need [5,6,32].

Endowed with benign biocompatibility, the piezocatalytic activities of KNN-based materials have recently been stressed on [22,27,34,35]. However, compared with lead-based materials, KNN-based materials in previous reports have relatively inferior piezoelectric properties (i.e., lower piezoelectric constant,  $d_{33}$ ), limiting their piezocatalytic activities. On consideration of the equation of  $d_{33} = 2Q\epsilon_0\epsilon_rP_r$  (where  $Q$ ,  $\epsilon_0$ , and  $\epsilon_r$  are electrostriction coefficient, space-free dielectric permittivity, and relative dielectric permittivity, respectively) [36,37],  $d_{33}$  hinges on

\* Corresponding authors.

E-mail addresses: [lvxiangscu@163.com](mailto:lvxiangscu@163.com) (X. Lv), [wujiagang0208@163.com](mailto:wujiagang0208@163.com), [msewujg@scu.edu.cn](mailto:msewujg@scu.edu.cn) (J. Wu).

<https://doi.org/10.1016/j.apcatb.2022.121471>

Received 27 January 2022; Received in revised form 28 April 2022; Accepted 1 May 2022

Available online 4 May 2022

0926-3373/© 2022 Elsevier B.V. All rights reserved.

the product of  $\epsilon_r$  and  $P_r$ . It has been reported that  $\epsilon_r$  highly depends on polarization rotation that is boosted in a mixed system consisting of two or more different crystallographic symmetries due to the reduced energy barrier for polarization rotation [8,38–40]. Therefore, modulating polarization rotation is highly promising for improving piezoelectric properties and resultant piezocatalytic activities. Considering the ferroelectric phase transition sequences of pristine KNN [8], we proposed to construct a room-temperature multiphase coexistence (i.e., a mixed system with different crystallographic symmetries) for promoting polarization rotation among different ferroelectric phases, by which we expected to improve the piezoelectric properties and resultant piezocatalytic activities of KNN materials, as schemed in Fig. 1.

To verify our concept, we chose  $(\text{Bi}_{0.5}\text{Na}_{0.5})\text{ZrO}_3$  (BNZ) and  $\text{Sb}^{5+}$  to shift  $T_{\text{O-T}}$  (orthorhombic-tetragonal phase transition temperature) and  $T_{\text{R-O}}$  (rhombohedral-orthorhombic phase transition temperature), respectively [41]. Thus, three typical KNN-based materials with different crystallographic symmetries are used in these work, that is,  $(\text{K}_{0.5}\text{Na}_{0.5})\text{NbO}_3$  (KNN),  $0.95(\text{K}_{0.48}\text{Na}_{0.52})\text{NbO}_3-0.05(\text{Bi}_{0.5}\text{Na}_{0.5})\text{ZrO}_3$  (KNN-BNZ), and  $0.96(\text{K}_{0.48}\text{Na}_{0.52})\text{Nb}_{0.955}\text{Sb}_{0.045}\text{O}_3-0.04(\text{Bi}_{0.5}\text{Na}_{0.5})\text{ZrO}_3$  (KNNS-BNZ) [9,42]. The experimental results well validate our concept. We achieved enhanced piezocatalytic activities and good circulation in the KNNS-BNZ sample possessing the most quantities of different crystallographic symmetries. We expounded the physical mechanism of the enhanced piezocatalytic activities from easier polarization rotation, carrier concentration, and the mechano-charge generation.

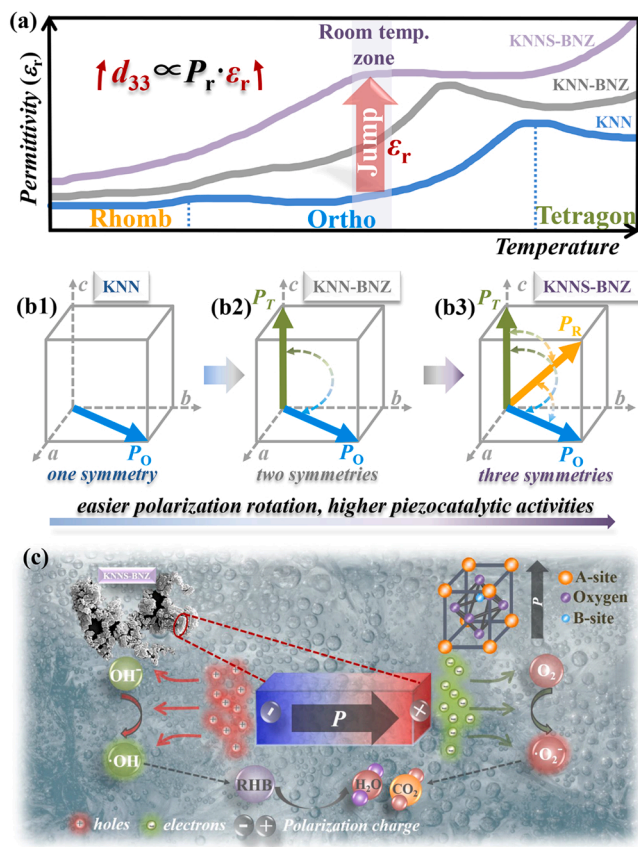


**Fig. 1.** Schematic diagrams of (a) temperature-dependent dielectric permittivity and (b1-b3) spontaneous polarization ( $P_s$ ) vectors for KNN, KNN-BNZ, and KNNS-BNZ materials. (c) Schematic diagram illustrating the generation of electrons and holes and their transferring for piezocatalysis.

## 2. Experimental procedure

### 2.1. Preparation of materials

We used the conventional solid-state sintering method to fabricate KNN, KNN-BNZ, and KNNS-BNZ powder samples. First, raw materials, including  $\text{K}_2\text{CO}_3$  (99.99%),  $\text{Na}_2\text{CO}_3$  (99.99%),  $\text{Nb}_2\text{O}_5$  (99.99%),  $\text{Sb}_2\text{O}_3$  (99.99%),  $\text{Bi}_2\text{O}_3$  (99.99%), and  $\text{ZrO}_2$  (99.99%) (Shanghai Aladdin Biochemical Technology Co., Ltd., CN), were weighted according to stoichiometric ratio and mixed with alcohol and  $\text{ZrO}_2$  balls in nylon jars for the subsequent 24-hour ball-milling. Then, these dried powders were calcined at  $650^\circ\text{C}$  for 120 min and high energy ball-milling for 5 h to refine powders. Next, these refined powders were heated at  $700^\circ\text{C}$  for 30 min to remove stress from ball-milling. Finally, the as-prepared powders were poled in a quartz mold under a direct current electric field of 8 kV/mm at  $30^\circ\text{C}$  for 3 h. Besides, we also prepared KNN, KNN-BNZ, and KNNS-BNZ bulk ceramics for measuring temperature-dependent dielectric properties [41].

### 2.2. Characterization

The powder samples' crystal structures were measured by using a high-resolution X-ray diffraction (XRD) apparatus (X' Pert Pro MPD, DY 120 PANalytical, Netherlands). X-ray photoelectron spectroscopy (XPS, XSAM 800) was used to detect the chemical state and valence band. DSC (METTLER TOLEDO-DSC3+) measurements and Raman spectroscopy (HORIBA-LabRAM) were conducted to confirm the phase structure of the powder samples. BET (ASAP 2460 Version 3.01) surface area measurements were conducted to investigate the surface area and pore distribution. LC-MS (PR-LCMS-2020) was conducted to analyze degradation products. The temperature-dependent dielectric permittivity ( $\epsilon_r$ ) of the bulk ceramics were characterized by a broadband dielectric spectrometer (Novocontrol Concept 80, Novocontrol, Germany), with a heating process from  $-150$ – $300^\circ\text{C}$ . The surface microstructure of the powder samples was collected by a scanning electron microscope (SEM) (JSM-7500, Japan). To detect the local piezoelectric response, the switching spectroscopy piezoresponse force microscopy (SS-PFM) loops were measured by using a commercial atomic force microscope (MFP-3D, Asylum Research, Goleta, CA) equipped with a conductive Pt-Ir coated cantilever (Nanosensors, Switzerland). To detect the powder samples' band gap, a UV-Vis spectrophotometer (UV-3600, Hitachi, Japan) was used to collect the UV-Vis diffuse reflectance spectra, and  $\text{BaSO}_4$  was used as the reference. To detect the charge transfer resistance on the electrode surface and the flat band potential and piezocurrent, the electrochemical experiments were used to test the Nyquist plots and Mott-Schottky plots. A CHI660E electrochemical workstation (Shanghai Chenhua Instrument Corporation, China) with a three-electrode system was used to test the electrochemical experiments. The working electrode, reference electrode, and counter electrode were the F-doped  $\text{SnO}_2$  (FTO) glass coated with a piezoelectric catalyst, Ag-AgCl electrode, and platinum electrode, respectively. The supporting electrolyte was  $\text{Na}_2\text{SO}_4$  (0.1 M) solution, and a variable power ultrasonic machine (40 kHz) was used to output mechanical vibration. EPR spectra (Bruker EMXplus X-band EPR spectrometer) were used to detect the reactive oxygen species.

### 2.3. PENG fabrication and characterization

The spin-casting method was used to fabricate PENG samples of PDMS-KNN, PDMS-KNN-BNZ, and PDMS-KNNS-BNZ. First, the PDMS solution was prepared by adding a curing agent into pristine PDMS (Polydimethylsiloxane; Sylgard 184, Dow Corning Corp., Auburn, MI) (the weight ratio of PDMS to curing agent was 10:1). Then, the KNN, KNN-BNZ, and KNNS-BNZ powders were mixed with the PDMS solution, with a weight ratio of PDMS solution to powders of 1:0.4. And then, the mixtures were stirred and then in ultrasonic for 30 min to disperse evenly. The as-prepared mixtures were spin-cast onto the glass plate at a

speed of 500 rpm-5 s-600 rpm-8 s and then cured at 100 °C for 3 h. Next, the as-prepared thick films were peeled off the glass plate and cut into squares of 1 cm × 1 cm. Square samples' surfaces were covered with Cu electrodes and Kapton films with a 0.4 cm × 0.4 cm hole in the middle to form the PENG device. Finally, the PENG device was poled under a direct current electric field of 10 kV/mm<sup>-1</sup> at 30 °C for 8 h. By applying a periodic vertical force of 25 N at a frequency of 40 kHz, the PENG devices output a constant and stable voltage. The vertical force is generated by using a pushing tester (WMUC512075-06-X). Digital oscilloscope (ROHDE & SCHWARZ, RTE 1054) and high impedance electrometer (Keithley 6514) were used to record the output voltage of the PENG.

#### 2.4. Piezocatalytic measurement

The piezocatalytic activities of KNN, KNN-BNZ, and KNNS-BNZ powder samples were characterized by the degradation of the typical dye rhodamine B (RhB) under ultrasonic vibration (40 kHz, 360 W). First, 0.2 g powder was mixed with 50 mL RhB (5 mg/L) in a beaker and stirred in dark for 30 min using a magnetic mixer to achieve the dissociation-adsorption equilibrium. Then, the beaker was fixed in an ultrasonic machine for piezoelectric catalytic degradation. The whole process is carried out in the dark and at around 25 °C by circulating the water to avoid disturbance from light and heat. To test the piezocatalytic activity, a 5 mL reaction solution was sucked out every 5 min, and the powder was separated by centrifugation. Then the concentration of dye aqueous solution was determined by a UV-Vis spectrophotometer.

#### 2.5. Phenomenological theory

According to Landau-Ginsburg-Devonshire phenomenological model, the density of Gibbs free energy for stress-free ferroelectric could be expressed as:

$$\begin{aligned} \Delta G = & \alpha_1 (P_1^2 + P_2^2 + P_3^2) + \alpha_{11} (P_1^4 + P_2^4 + P_3^4) + \alpha_{12} (P_1^2 P_2^2 + P_1^2 P_3^2 + P_2^2 P_3^2) \\ & + \alpha_{112} [P_1^4 (P_2^2 + P_3^2) + P_2^4 (P_1^2 + P_3^2) + P_3^4 (P_1^2 + P_2^2)] + \alpha_{111} (P_1^6 + P_2^6 + P_3^6) \\ & + \alpha_{123} P_1^2 P_2^2 P_3^2 - E_1 P_1 - E_2 P_2 - E_3 P_3 \end{aligned}$$

Where  $P_i$  ( $i = 1, 2, 3$ ) and  $E_i$  ( $i = 1, 2, 3$ ) are the polarization and the corresponding applied external electric-field, respectively.  $\alpha_1$ ,  $\alpha_{11}$ ,  $\alpha_{12}$ ,  $\alpha_{111}$ ,  $\alpha_{112}$  and  $\alpha_{123}$  are Landau energy coefficients, which determine the ferroelectric transition, the stability of ferroelectric phases, and the thermodynamic behavior of ferroelectric phases. Based on the dielectric properties and phase transition temperature of KNN and KNNS-BNZ bulk ceramics, the Landau coefficients are set as follows:

$$\alpha_1 = 2.273 \times 10^6 (\text{tem}-498) \text{ C}^{-2} \text{ m}^2 \text{ N},$$

$$\alpha_{11} = 2.647 \times 10^6 (\text{tem}-508) \text{ C}^{-4} \text{ m}^6 \text{ N},$$

$$\alpha_{12} = 9.66 \times 10^8 \text{ C}^{-4} \text{ m}^6 \text{ N},$$

$$\alpha_{111} = (-5.86 \times 107 (\text{tem}-508) - 2.81 \times 10^9) \text{ C}^{-6} \text{ m}^{10} \text{ N},$$

$$\alpha_{112} = -1.99 \times 10^9 \text{ C}^{-6} \text{ m}^{10} \text{ N},$$

$$\alpha_{123} = 1.55 \times 10^{10} \text{ C}^{-6} \text{ m}^{10} \text{ N}.$$

### 3. Results and discussion

#### 3.1. Phase structure

Firstly, we checked the phase structure of KNN, KNN-BNZ, and KNNS-BNZ powders using XRD patterns (Fig. 2(a1)), focusing on whether the phase structure evolves as we expected. All powder samples' diffractions get widened compared with their bulk ceramic counterparts due to the grain size refinement [41]. KNN powders show a

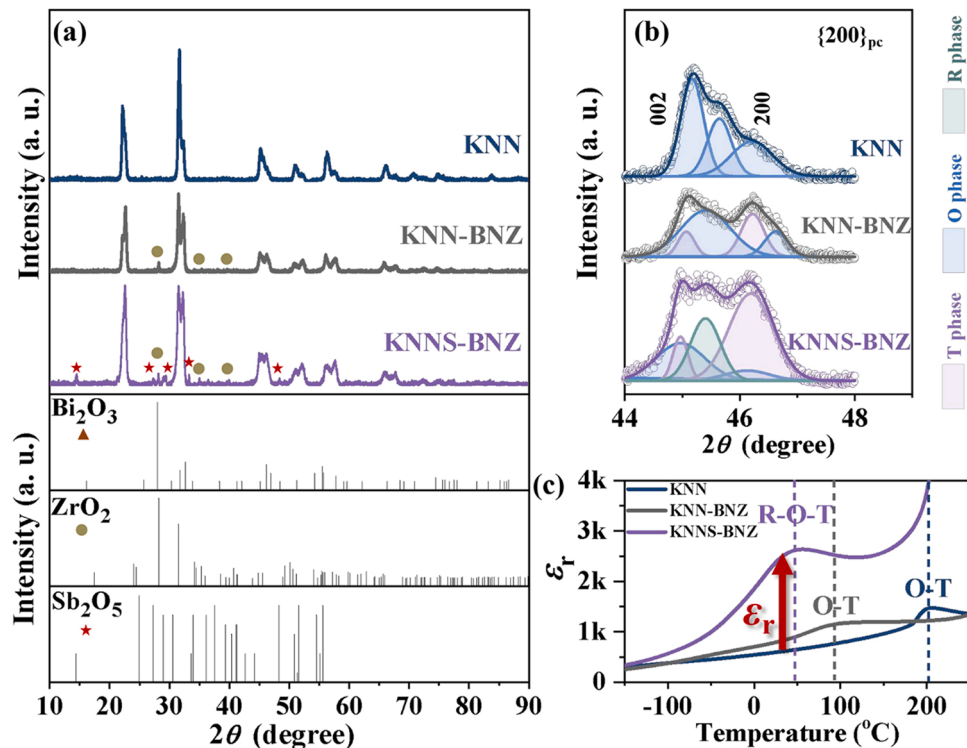


Fig. 2. Room-temperature XRD patterns of KNN, KNN-BNZ, and KNNS-BNZ powders with  $2\theta = 10\text{--}90^\circ$  (a) and  $2\theta = 44\text{--}48^\circ$  (b). (c) Temperature-dependent  $\epsilon_r$  of KNN, KNN-BNZ, and KNNS-BNZ bulk ceramics.

typical perovskite structure without any detectable secondary phases [8], while the other two powders show a typical perovskite structure coexisting with some minor secondary phases, which are due to the incompletely reacted  $\text{ZrO}_2$  and  $\text{Sb}_2\text{O}_5$ . To further discuss the phase structure evolution,  $\{200\}_{\text{pc}}$  diffraction is fitted (Fig. 2(a2)). For KNN powders, the intensity of  $(002)_{\text{pc}}$  peak (i.e.,  $I_{002}$ ) is higher than that of  $(200)_{\text{pc}}$  peak (i.e.,  $I_{200}$ ), suggesting a dominating O phase at room temperature [43]. For KNN-BNZ and KNNS-BNZ powders,  $I_{002}$  decreases and  $I_{200}$  increases, indicating the involvement of a tetragonal (T) phase [44]. The comparable  $I_{002}$  and  $I_{200}$  in KNN-BNZ powders suggest an O-T coexistence phase at room temperature [45]. While a rhombohedral (R) phase appears as a single peak in  $\{200\}_{\text{pc}}$  diffraction of KNNS-BNZ powders, suggesting an R-O-T coexistence phase at room temperature [45,46]. Therefore, as we expected, we successfully prepared KNN-based powders containing different crystallographic symmetries.

To further understand the phase structure evolution and check whether the dielectric response is enhanced as we expected, we measured temperature-dependent dielectric permittivity ( $\epsilon_r$ ) of their bulk ceramics (Fig. 2c). With the addition of  $(\text{Bi}_{0.5}\text{Na}_{0.5})\text{ZrO}_3$ ,  $T_{\text{O-T}}$  gradually decreases and moves towards room temperature, thus forming an O-T coexistence phase in KNN-BNZ ceramics. Then, co-doping  $(\text{Bi}_{0.5}\text{Na}_{0.5})\text{ZrO}_3$  and  $\text{Sb}^{5+}$  into KNN simultaneously moves  $T_{\text{R-O}}$  and  $T_{\text{O-T}}$  to room temperature, thus forming an R-O-T coexistence phase in KNNS-BNZ ceramics. Therefore, the evolutions of powder samples' phase structures are well consistent with those of bulk ceramics [9,42]. Of particular importance is that the room-temperature  $\epsilon_r$  is significantly improved in KNNS-BNZ ceramics, much superior to that of KNN-BNZ and KNN ceramics. Besides, KNN-BNZ ceramics also exhibit a higher room-temperature  $\epsilon_r$  than KNN ceramics due to an O-T coexistence phase. Therefore, the mixed system with different crystallographic symmetries does promote polarization rotation and thus enhances  $\epsilon_r$ . Moreover, Raman spectra and DSC curves of the powder samples further characterized the phase structure evolution (Fig. S5).

To further identify the perovskite structure and the other secondary phases, we checked the chemical composition and the elements' chemical states on the surface of the powder. All elements including Sb, O, Nb, K, Bi, Zr, and Na are well detected, coinciding with the raw materials (see Fig. 3 and Fig. S1). The high-resolution spectra of O 1s and Sb 3d are shown in Fig. 3(a). For KNNS-BNZ powders, Sb 3d shows a strong peak at 538.939 eV, which is mainly ascribed to  $\text{Sb}^{5+}$  entering to KNN lattice, while the secondary phase  $\text{Sb}_2\text{O}_5$  also has some influence.

The O 1s peaks for all powder samples can be fitted to two peaks, marked as O 1s<sup>1</sup> and O 1s<sup>2</sup>. O 1s<sup>1</sup> is ascribed to the oxygen vacancy, and O 1s<sup>2</sup> stems from the oxygen in the lattice [30]. Thus, the ratio of O 1s<sup>2</sup> to O 1s<sup>1</sup> can reflect the quality of the obtained perovskite structure to a large degree [47]. Fig. 3(f) shows the ratio of the oxygen in the lattice. The oxygen in the lattice ratio gradually increases with the increasing degree of doping, indicating that co-doping BNZ and  $\text{Sb}^{5+}$  not only alters the phase structure but also is more conducive to the formation of the perovskite structure. The high-resolution Nb 3d, K 2p, Bi 4f, and Zr 3d spectra are shown in Fig. 3(b-e). Nb 3d, K 2p, and Bi 4f peaks split into Nb 3d<sub>3/2</sub>, Nb 3d<sub>5/2</sub>, K 2p<sub>1/2</sub>, K 2p<sub>3/2</sub>, Bi 4f<sub>5/2</sub>, and Bi 4f<sub>7/2</sub>, corresponding to B-site and A-site ions in the perovskite structure, respectively. Zr 3d peaks split into Zr 3d<sub>3/2</sub> and Zr 3d<sub>5/2</sub>, and exist mainly in the form of B-site ions in the perovskite structure and the form of  $\text{ZrO}_2$  a bit. In addition, the change of elements' binding energies is mainly related to ion doping substitution [27]. Therefore, all elements could be detected, and O atoms mainly exists in the lattice of the perovskite structure.

### 3.2. Surface morphology

Surface morphology is important for catalytic efficiency, so we next explored the influence of composition on morphology (Fig. 4). All powder samples display a bimodal distribution, containing both large and small grains. KNN powders show small particle clusters, accompanied by fewer large grains, and their grain size significantly decreases compared with KNN bulk ceramics because of lacking high-temperature sintering that is helpful for mass transmission and facilitates grain growth [48]. Compared with KNN powders, KNN-BNZ and KNNS-BNZ powder samples show more large grains, which is caused by the addition of Bi, Zr, and Sb promoting grain growth [42]. Although the increased grain size was reported to be detrimental to piezocatalytic activities to some degree, it can significantly boost the piezoelectric properties because of promoting polarization rotation, resulting in a trade-off relationship [35,42,49]. In addition, the BET measurements also reveal a smallest surface area in the KNNS-BNZ sample (Fig. S8). But a highest normalized  $k$  value is observed in the KNNS-BNZ sample, indicating that the increased piezoelectric properties are the main driver of the high catalytic activities.

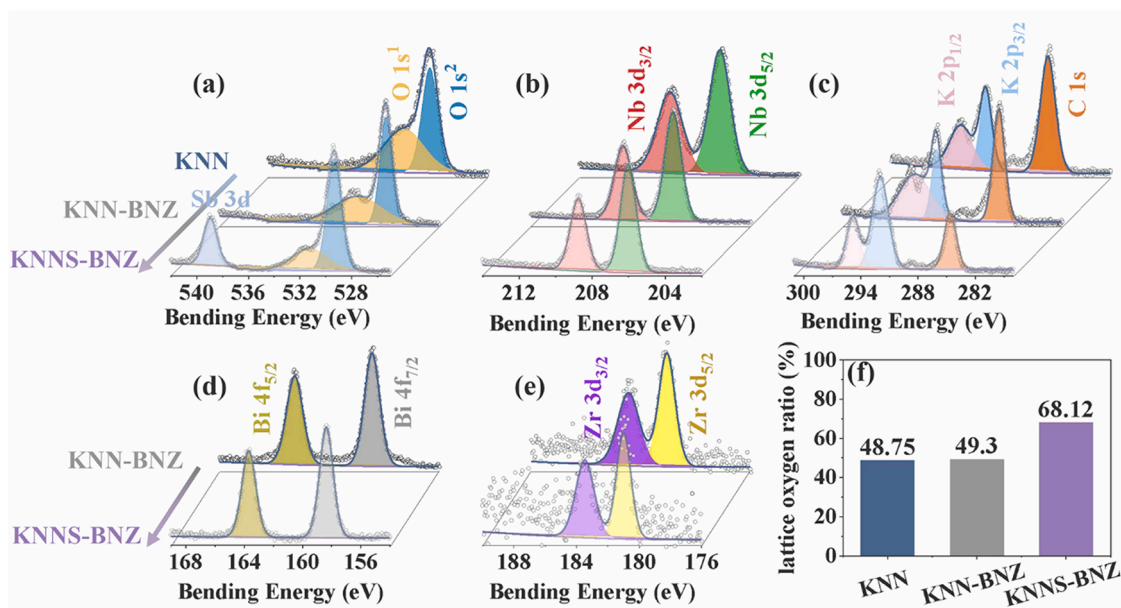


Fig. 3. The valence state of Sb 3d and O 1s (a), Nb 3d (b), K 2p and C 1s (c), Bi 4f (d), and Zr 3d (e). (f) The lattice oxygen fraction of three powder samples.



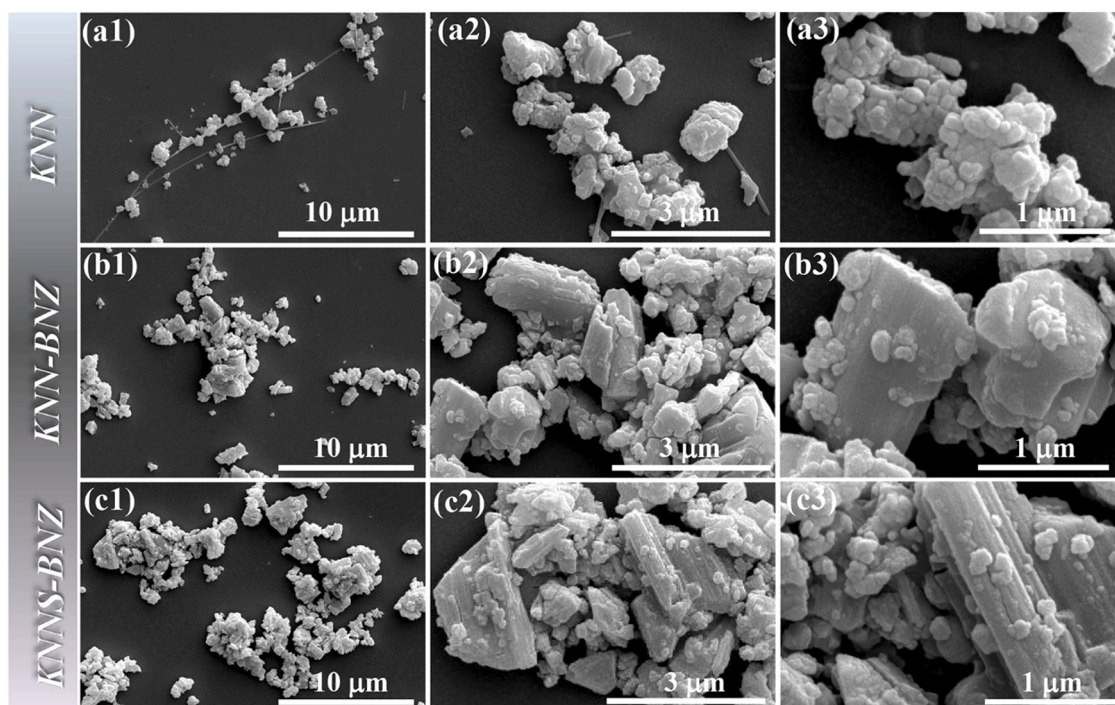


Fig. 4. SEM surface images with different magnifications of (a1)-(a3) KNN, (b1)-(b3) KNN-BNZ, and (c1)-(c3) KNNS-BNZ powder samples.

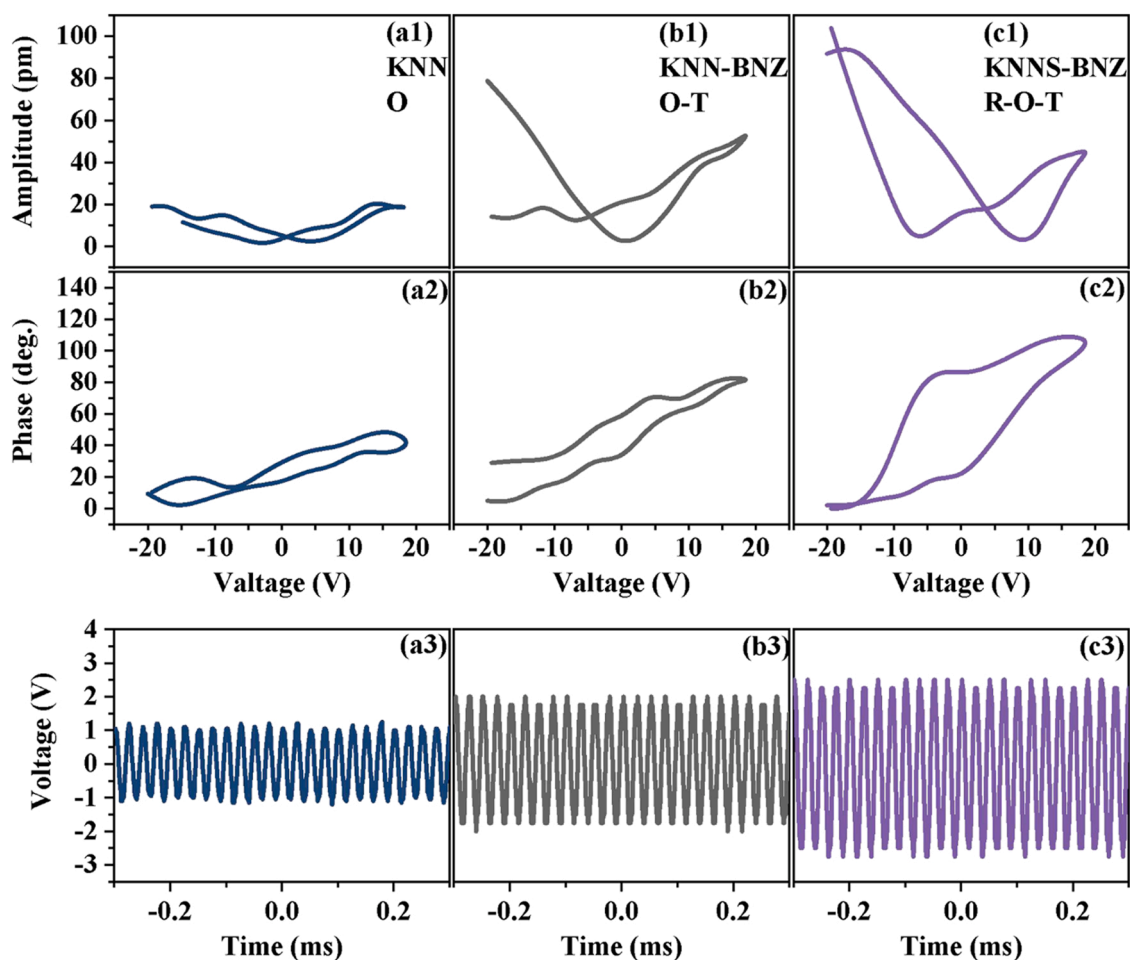


Fig. 5. SS-PFM measurements for (a1, a2) KNN, (b1, b2) KNN-BNZ, and (c1, c2) KNNS-BNZ powder samples. The time-dependent output voltage for PENGs with (a3) KNN, (b3) KNN-BNZ, and (c3) KNNS-BNZ powders.

### 3.3. Piezoelectric properties

Since we have obtained the mixed system containing different ferroelectric phases and observed the increased  $\epsilon_r$ , it is needed to evaluate whether the piezoelectric properties are enhanced as we expected. By applying a local voltage of 20 V on the powder surface, the local piezoelectric response can be detected (Fig. 5(a1-c2)). The addition of BNZ and/or  $\text{Sb}^{5+}$  increases the amplitude of SS-PFM loops, suggesting enhanced local piezoelectricity [50,51]. In particular, both the amplitude and the phase contrast reach the maximum in KNN-BNZ powders, manifesting the highest local piezoelectric response [51]. Additionally, it is worth noting that the non-closed SS-PFM curves of the powder samples are mainly due to the weak contact between the PFM tip and the powders during the test, and the powders are prone to slight displacement, which also exist in other systems [28,31,52]. To further demonstrate the piezoelectric properties, we measured the voltage-time curves by using the PENG device (Fig. 5(a3-c3)). The output voltage of PENG is positively proportional to the piezoelectric properties of piezoelectric powder samples [11]. Fig. 5(a3-c3) show that the higher the local piezoelectric response is, the larger the output voltage is. In particular, compared with the 1.2 V output voltage of KNN-based PENG, the 1.8 V output voltage of KNN-BNZ increases by 50%, and the 2.75 V output voltage of KNN-BNZ increases by 129%. Therefore, modulating polarization rotation indeed effectively promotes the piezoelectric properties, well validating our expectation.

### 3.4. Piezocatalytic activities

We have demonstrated the phase structure, microstructure, and piezoelectric properties of the powder samples. Exhilaratingly, the easier polarization rotation in the mixed system consisting of two or more crystallographic symmetries does enhance the piezoelectric properties. We then checked whether the piezocatalytic activities are significantly enhanced as we expected. Poling is a necessary process for inducing net piezoelectric properties in polycrystalline piezoelectric ceramics [8]. Therefore, we contrasted the piezocatalytic activities

depending on the composition and poling condition (unpoled and poled powders are abbreviated as UP and P, respectively) (Fig. 6(a1)). To exclude the vibration degradation effect to RhB, we also measured the self-degradation of RhB in the same ultrasonic environment and found that the self-degradation is very low (Fig. 6(a1)). By contrast, the powder samples significantly enhance the catalytic activities. Of particular importance is that KNN-BNZ powders show the best piezocatalytic activities among three powder samples, especially for the poled KNN-BNZ powders (Fig. 6(a1)).

Generally, the piezocatalytic activities obey the Langmuir-Hinshelwood model, as shown in Eq. (1) [3,27].

$$C = C_0 \bullet e^{-kt} \quad (1)$$

Where  $C$ ,  $C_0$ , and  $k$  are the concentration at the ultrasonic time of  $t$ , the initial concentration of dye solution, and the reaction rate constant, respectively [3,27]. Thus, we linearly fitted the  $\ln(C_0/C)$  and  $t$  to obtain the  $k$  values (Fig. 6(a2, c)). Compared with UP-KNN powders, the  $k$  values of UP-KNN-BNZ and UP-KNN-BNZ powders increase by 72% and 83%, which is related to the weak poling effect caused by the ultrasonic-induced local high pressure. After poling, the  $k$  values are significantly improved, and reach the maximum of  $0.091 \text{ min}^{-1}$  in P-KNN-BNZ powders, 2.12 times more than that of P-KNN powders.

Since a small number of secondary phases, associated with the incompletely-reacted metal oxides, are observed in KNN-BNZ and KNN-BNZ powders, it is necessary to find out whether these secondary phases affect the catalytic activities. Thus, we carried out comparative experiments by adding  $\text{Bi}_2\text{O}_3$ ,  $\text{ZrO}_2$ , and  $\text{Sb}_2\text{O}_3$  (abbreviated to B, Z, and S) into UP-KNN powders (Fig. 6(b1, b2)). Compared with UP-KNN powders, the decomposition ratio at 30 min of UP-KNN+B+Z and UP-KNN+B+Z+S powders is slightly improved, which may be related to the mechano-catalytic effect [53,54]. The degradation ratio of UP-KNN+B+Z and UP-KNN+B+Z+S powders is higher than that of UP-KNN powders but lower than that of UP-KNN-BNZ and UP-KNN-BNZ powders, indicating that the incompletely-reacted metal oxides slightly contribute to the ultrasonic-catalytic activities.

Friction between different electronegativity materials would result

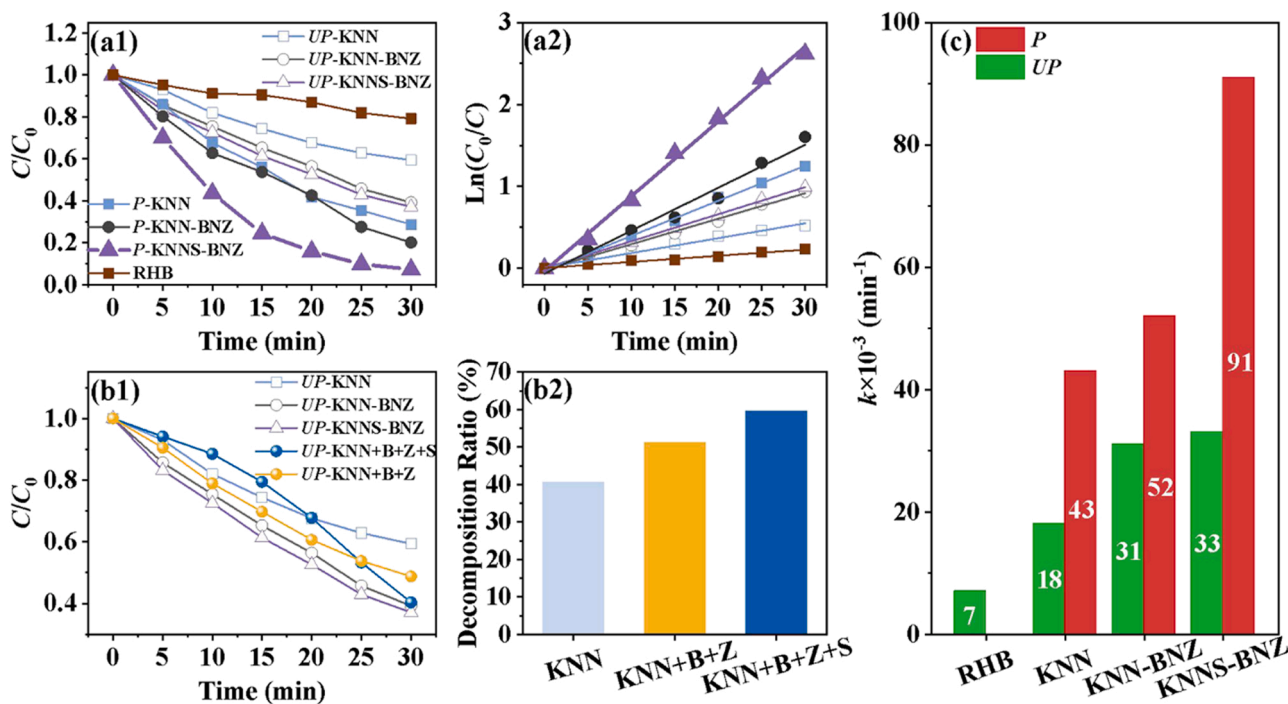


Fig. 6. (a1)  $C/C_0$  and (a2)  $\ln(C_0/C)$  of the P- and UP- powder samples as a function of time. (b1)  $C/C_0$  of UP-KNN-based powders and UP-KNN powders containing metal oxides. (b2) Degradation ratio of UP-KNN, UP-KNN+B+Z, and UP-KNN+B+Z+S powders at 30 min (c)  $k$  values of the P- and UP- powder samples. All data are read from Fig. S2.

in charge transferring from low-electronegative materials to high-electronegative ones [55]. We calculated the materials' electronegativities by the following Eq. (2) [55].

$$\chi_{\text{material}} = [\chi_{\text{M}}^m(\chi_{\text{O}})^n]^{1/(m+n)} \quad (2)$$

Where  $\chi_{\text{material}}$  is the electronegativity of the material. The material is abbreviated to  $\text{M}_m\text{O}_n$ . According to Eq. (2), the electronegativities of  $\text{Bi}_2\text{O}_3$ ,  $\text{ZrO}_2$ ,  $\text{Sb}_2\text{O}_5$ , KNN, KNN-BNZ, and KNNS-BNZ are calculated to be 2.71, 2.51, 2.97, 2.26, 2.26, and 2.26, respectively. The electronegativity of KNN, KNN-BNZ, and KNNS-BNZ is almost equivalent and relatively small compared to the metallic oxides. Thus, the free charge could be transferred from KNN to metallic oxides through mechano-ultrasonic vibration, partly contributing to the ultrasonic-catalytic activities. Ultrasonic catalytic activities of pure oxides are also

investigated (Fig. S6), and compared with piezocatalytic activities, the mechano-catalytic effect of the mixed oxide system is very low. Therefore, it should be pointed out that the enhanced piezoelectric properties govern the catalytic activities.

The cycle stability of piezocatalysis is crucial for practical applications. Therefore, we conducted piezocatalytic activities measurements for four cycles (Fig. 7(a, b)). To avoid the effect of adsorption, the powder samples are washed with deionization water and dried before the next cycle. After four times cycles, the piezocatalytic activities maintain a high degradation ratio of 89%, which is inseparable from the structural stability of the powders. Then, we identified which free radical plays the major role in *P*-KNNS-BNZ piezocatalytic activities by adding free radical scavengers, including hydroxyl radicals ( $\cdot\text{OH}$ ) scavengers (TBA), holes ( $\text{h}^+$ ) scavengers (EDTA-2Na), and superoxide

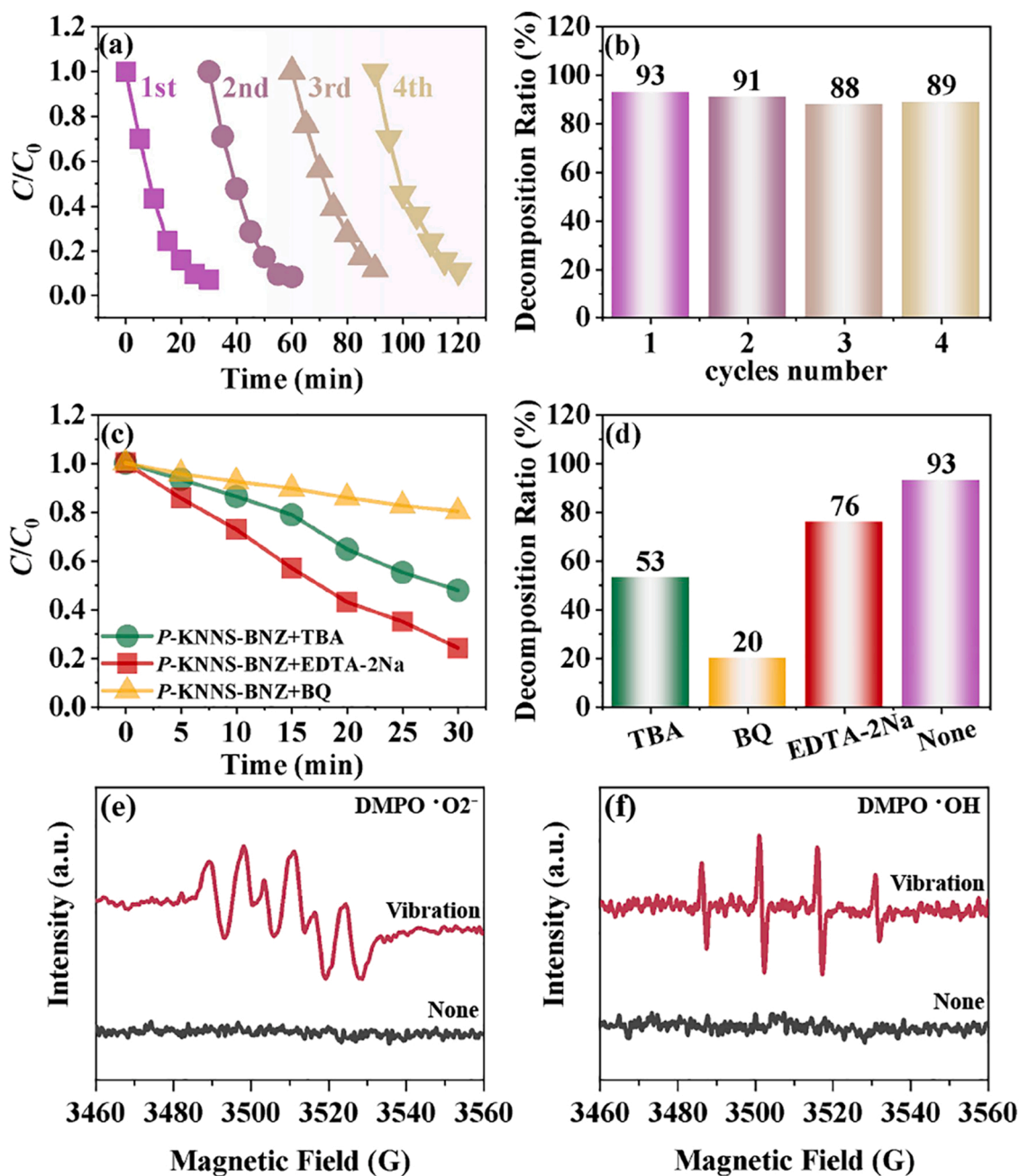


Fig. 7. (a)  $C/C_0$  of *P*-KNNS-BNZ powders for four times cycles and (b) the corresponding degradation ratio at 30 min (c) Radical trapping experiments of *P*-KNNS-BNZ powders and (d) the corresponding degradation ratio at 30 min. The piezocatalytic activities are read from Fig. S3. EPR spectra of (e)  $\text{DMPO} \cdot \text{O}_2^-$  and (f)  $\text{DMPO} \cdot \text{OH}$  using *P*-KNNS-BNZ as piezocatalyst.



radicals ( $\cdot\text{O}_2$ ) scavengers (BQ) (Fig. 7(c, d)) [2,27]. By comparing the degradation ratio at 30 min of different free radical scavengers, it is found that the degradation ratio of BQ is the lowest, indicating that  $\cdot\text{O}_2$  is the most crucial free radical and  $\cdot\text{OH}$  also contributes part of piezocatalytic activities. Adding EDTA-2Na has a negligible influence on the piezocatalytic activities, indicating that  $\text{h}^+$  almost has no contribution. Moreover, EPR spectra were conducted to further detect the reactive oxygen species including  $\cdot\text{O}_2$  and  $\cdot\text{OH}$  (Fig. 7(e, f)).  $\cdot\text{O}_2$  and  $\cdot\text{OH}$  are detected after vibration but not be detected without vibration, indicating that two free radicals are generated under the combined action of piezoelectric powders and ultrasound [27]. Therefore, we obtained a stable piezocatalyst (i.e., P-KNNS-BNZ powders), and  $\cdot\text{O}_2$  is their most important free radical.

### 3.5. Physical mechanisms

Since the energy band structure and resistance are crucial for catalytic activities, we then determined the energy band structure and

analyzed the charge transfer resistance on the electrode surface and the piezocurrent response of the poled powder samples. First, the VB values of KNN, KNN-BNZ, and KNNS-BNZ powders are 2.07 eV, 2.20 eV, and 2.34 eV, respectively (Fig. 8(a)) [56]. Then, the positive slope of the Mott-Schottky curves indicates that poled KNN, KNN-BNZ and KNNS-BNZ powders are *n*-type semiconductors (Fig. 8(b1-b3)) [24]. The Fermi level ( $E_f$ ) generally corresponds to the flat band potential ( $V_{fb}$ ), which could be calculated by extrapolating the linear part of the Mott-Schottky curves to the potential axis [27].  $E_f$  of KNN, KNN-BNZ, and KNNS-BNZ are  $-0.41$  V,  $-0.36$  V, and  $-0.36$  V (vs Ag/AgCl electrode), respectively, corresponding to  $-0.21$  V,  $-0.16$  V, and  $-0.16$  V (vs NHE potential), respectively. Then, the band gap ( $E_g$ ) is determined by the UV-Vis diffuse reflectance spectra in Fig. 8(c) and calculated from the inset Tauc plot using the Tauc equation [57].

$$(\alpha h\nu)^{1/n} = A(h\nu - E_g) \quad (3)$$

Where  $\alpha$ ,  $h$ , and  $\nu$  represent the absorption coefficient, Planck's constant,

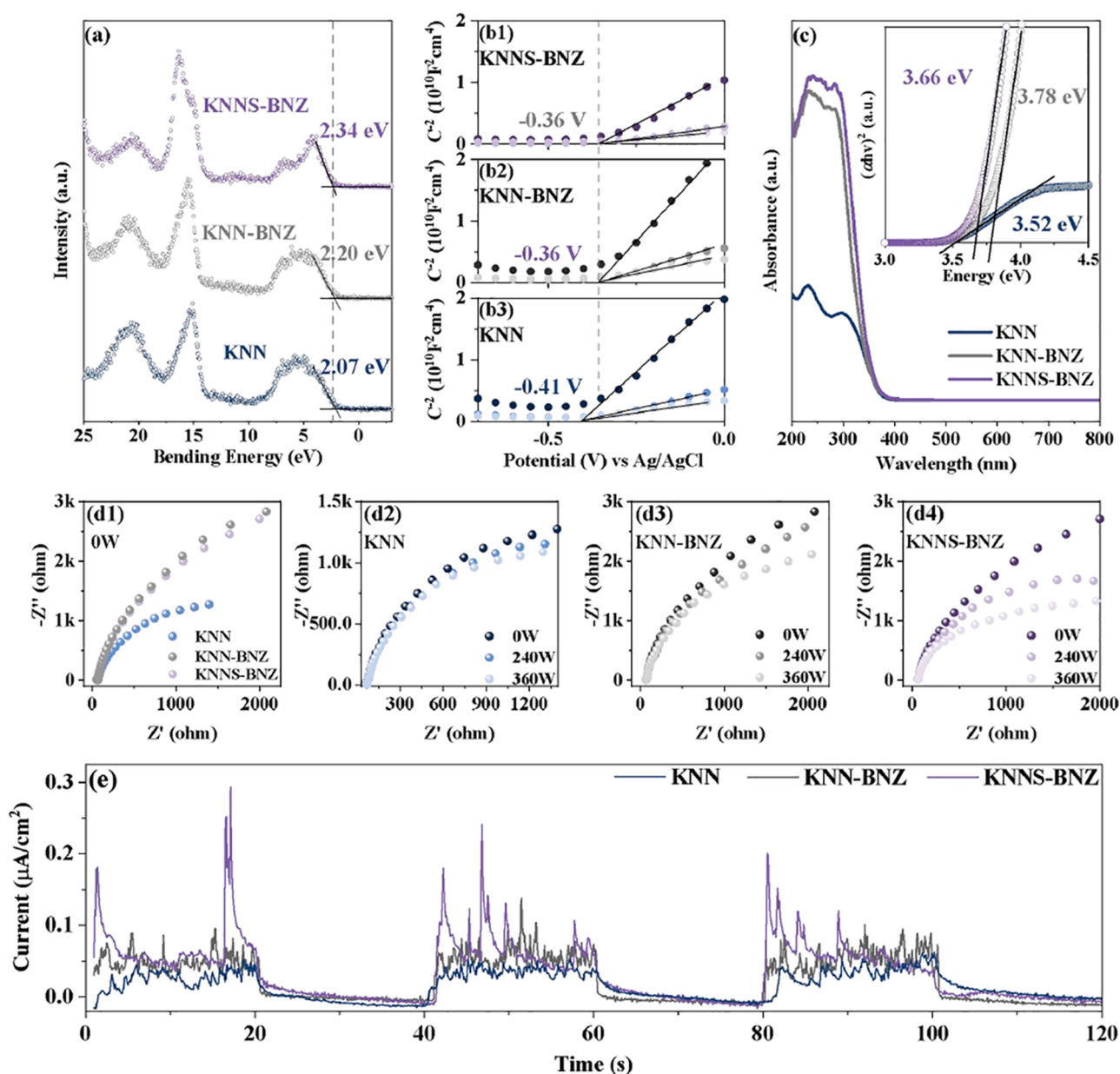


Fig. 8. (a) VB-XPS spectra. (b1-b3) Mott-Schottky curves. (c) UV-Vis diffuse reflectance spectra and the inset is the Tauc plot. (d1-d4) EIS Nyquist plots of three powder samples at different powers. (e) Piezocurrent responses of different samples.



and the incident light frequency, respectively.  $A$  is a constant, and  $n$  is 1/2 for direct band gap semiconductors [57]. Hence,  $E_g$  could be calculated by extrapolating the linear part of the Tauc plot to the energy axis, and those of KNN, KNN-BNZ, and KNNS-BNZ are 3.52 eV, 3.78 eV, and 3.66 eV, respectively. According to the above VB and  $E_g$ , we calculated the conduction band (VB) to be 2.07 eV, 2.20 eV, and 2.34 eV, respectively, for KNN, KNN-BNZ, and KNNS-BNZ powders.

The energy band structure of KNN, KNN-BNZ, and KNNS-BNZ powders are plotted in Fig. S4. Compared with KNN powders,  $E_g$  values of KNN-BNZ and KNNS-BNZ powders are increased because of doping BNZ and  $Sb^{5+}$ . Besides, the incompletely-reacted  $ZrO_2$  and  $Sb_2O_5$  also have a slight effect. The higher  $E_g$  value in KNNS-BNZ powders indicates that the free charges are more difficult to excite from CB to VB, and thus the intrinsic carrier concentration is lower and can be neglected at room temperature [58]. Since  $E_f$  is above the midline of CB and VB ( $E_i$ ), the doping impurity ionization contributes the most of the carrier concentration. More importantly, compared with KNN and KNN-BNZ powders, the  $E_f$  value of KNNS-BNZ powders is closer to CB, indicating KNNS-BNZ is a stronger  $n$ -type semiconductor [58]. The CB and VB of a stronger  $n$ -type semiconductor have the most electrons and the band is filled with more electrons, thus the concentration of doping impurity ionization carriers ( $N_D$ ) is also higher.  $N_D$  is determined by the following Eq. (4) [58]:

$$\frac{1}{C^2} = \left( \frac{2}{\epsilon \epsilon_0 A^2 e N_D} \right) \left( V - V_{fb} - \frac{k_B T}{e} \right) \quad (4)$$

Where  $C$ ,  $\epsilon$ ,  $\epsilon_0$ ,  $A$ ,  $e$ ,  $V$ ,  $k_B$ , and  $T$  represent the interfacial capacitance, the dielectric constant, the permittivity of free space, the interfacial area, the electronic charge, the applied potential, Boltzmann's constant, and the environment temperature, respectively. We can neglect the  $\frac{k_B T}{e}$  because it is small enough at room temperature, resulting in  $N_D$  inversely proportional to the slope of the Mott-Schottky curves. Thus, compared with KNN and KNN-BNZ powders,  $N_D$  of KNNS-BNZ powders is the highest. Because of the negligible intrinsic carrier concentration at room temperature, KNNS-BNZ powders have the most carrier concentration, which is beneficial to its piezocatalytic activities.

Then we studied the dynamic process of piezocatalysis by studying the dynamic change of impedance with ultrasonic power. First, Fig. 8 (d1) shows the EIS Nyquist plots at 0 W. In general, a smaller arc in the EIS Nyquist plot indicates a lower charge transfer resistance, which is related to carrier concentration and carrier mobility [2,58]. For KNNS-BNZ powders, although the carrier concentration is the maximum, the charge transfer resistance is not the minimum, which results from its lower carrier mobility. Then, when we applied ultrasound to the poled KNN, KNN-BNZ, and KNNS-BNZ powders, the charge transfer resistance decreases with increasing ultrasonic power, which is related to the built-in electric field allowing the carrier to migrate to the surface more efficiently [27]. More importantly, the reduction of charge transfer resistance with increasing ultrasonic power is the largest for poled KNNS-BNZ powders, indicating that the enhanced piezoelectric properties do facilitate more charge transferring to the surface faster, well validating our concept.

Moreover, the transient piezoelectric current density obtained by turning on and off the ultrasound was used to further demonstrate the improvement in catalytic activities (Fig. 8(e)). For KNN samples, the piezo-current is weak. By contrast, the powder samples of KNN-BNZ and KNNS-BNZ significantly enhanced the piezo-current, indicating more effective charge separation and transmission [59]. Therefore, the improvement in catalytic activities is due to the regulation of polarization rotation.

Finally, we summarized the piezocatalytic activities and mechanisms based on the abovementioned results and analysis. First, we compared the  $k$  values of this work ( $P$ -KNNS-BNZ powders) with those of other representative perovskite piezoelectric materials (Fig. 9(a)) [27–30,35,60]. Among KNN-based materials, our poled KNNS-BNZ powders show a

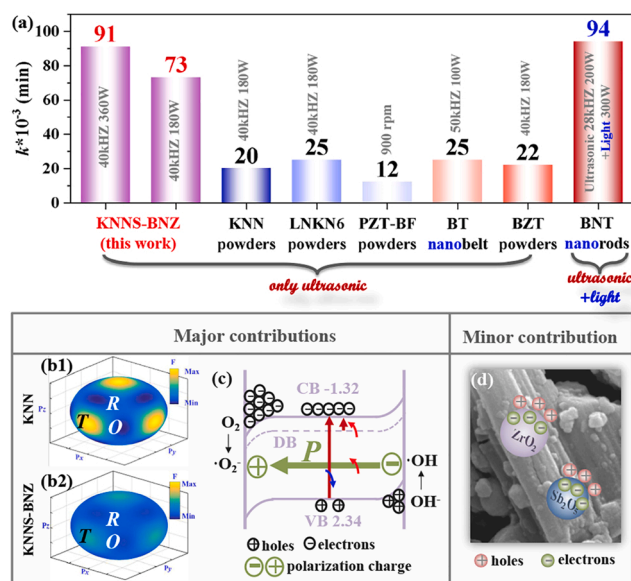


Fig. 9. (a) Comparison of  $k$  values of piezocatalytic activities using different piezoelectric materials. the concentration of RhB is 5 mg/L except for 10 mg/L for PZT-BF powders and BT nanobelt. Phenomenological theory simulations for (b1) KNN and (b2) KNNS-BNZ powders. (c) Schematic diagram illustrating the electron and hole generation, transfer, and application for piezocatalysis. (d) Schematic diagram illustrating mechano charge generation.

superior  $k$  value. Compared with other typical perovskite piezoelectric materials, our results still have advantages. In particular, we achieved a similar  $k$  value with BNT nanorods ultrasonic-photocatalysis [60]. More importantly, the preparation of our powder samples is relatively easier and cheaper than other nanobelts or nanorods, promising for practical applications. Therefore, the superior piezocatalytic activities in  $P$ -KNNS-BNZ powders primarily originate from the easier polarization rotation and resultantly improved carrier concentration, accompanied by the trace of the mechano-charge generation. The increased polarization charge hinges on the piezoelectric properties enhanced by the easier polarization rotation, which is achieved by constructing the mixed system consisting of two or more crystallographic symmetries at room temperature [9,39]. To show the easier polarization rotation vividly, we conducted the phenomenological theory for KNN and KNNS-BNZ powders (Fig. 9(b1, b2)) [38]. For KNN powders, the energy of the R, O, T phases are much different. The T phase exhibits the highest energy, while the O phase possesses the lowest one, indicating that the O phase is the most stable. For KNNS-BNZ powders, the energy barrier among R, O, and T phases is significantly fattened compared with that of KNN, indicating the stable mixed system and easier polarization rotation [38]. In addition, we also carried out LC-MS test on the degradation products, which confirmed that RhB was gradually degraded into small molecules (Figs. S9 and S10, Table S1). Fig. 9(c) shows the band gap structure of KNNS-BNZ powder samples. Although  $E_g$  is increased by dopants and metal oxides, we introduced donor band through doping and improved carrier concentration by promoting  $N_D$ , which is beneficial to the catalytic reaction. When ultrasonic waves were applied on the surface of the grain, the polarization strength ( $P$ ) will change periodically with the frequency of ultrasonic waves. So, the polarization charge also changes periodically, and a steady flow of electrons and holes are generated to counteract the polarization charge. The potential drops on the side of the grain surface where the polarization charge is positive, so that the potential on the grain surface is lower than that in the grain, and the potential bends down on this side, thus allowing the electrons to gather. By contrast, the grain surface with negative polarization charge aggregates holes. Moreover, we also expounded the effect of poling, ultrasound on  $P$ , and the relationship between polarization charge, free

electron holes, and absorbed species related shielding charge (Fig. S11). For KNNS-BNZ powders, as an *n*-type semiconductor,  $N_p$  contributes more electrons. In this reaction system, electron-related  $\cdot O_2$  is the main free radical, and hole-related  $\cdot OH$  is the secondary free radical. Similar to other works,  $h^+$  almost plays no role in RhB piezocatalytic reaction [27,58].

The mechanism of generating mechano-charge is shown in Fig. 9(d). When ultrasonic waves are applied to KNNS-BNZ powders,  $ZrO_2$  and  $Sb_2O_5$  particles will collide with KNNS-BNZ powders and realize charge separation. The high- electronegativity  $ZrO_2$  and  $Sb_2O_5$  attract electrons from the low-electronegativity KNNS-BNZ powders' surface to achieve charge separation, which could also react with  $O_2$  and  $OH^-$  to produce free radicals and be used for catalysis.

#### 4. Conclusion

In this work, we proposed enhancing the piezocatalytic activities of KNN-based materials by modulating the polarization rotation and validated our concept in three typical KNN-based powders with different crystallographic symmetries, that is, KNN with an O phase, KNN-BNZ with an O-T coexistence phase, and KNNS-BNZ with an R-O-T coexistence phase. We demonstrated the evolutions of the phase structure and verified the enhanced piezoelectric properties in KNNS-BNZ powders by SS-PFM and PENG measurements. In poled KNNS-BNZ powders, we obtained the improved *k* value of  $0.091 \text{ min}^{-1}$ , 2.12 times more than that of poled KNN ones, and superior to other representative perovskite piezoelectric materials. The superior catalytic activities are attributed to the synergistic effects. First, the enhanced piezoelectric properties associated with the easier polarization rotation govern the catalytic activities. Then, its carrier concentration increases, which is beneficial to catalysis. In addition, the mechano-charge generation also slightly contributes to catalysis. Therefore, this work would promote the development of lead-free piezoelectric materials for piezocatalysis.

#### CRedit authorship contribution statement

**Xi-xi Sun:** Investigation, Data curation, Methodology, Software, Writing – original draft, Visualization. **Xiang Lv:** Conceptualization, Formal analysis, Resources, Writing – review & editing, Supervision. **Ruichen Li:** Methodology, Software, Visualization, Writing – review & editing. **Zhiwei Yang:** Visualization, Writing – review & editing. **Nan Zhang:** Methodology, Software. **Chao Wu:** Methodology, Software. **Junhua Li:** Methodology, Software. **Yulin Chen:** Methodology, Software. **Qiang Chen:** Methodology, Software. **Jing Zhang:** Visualization, Writing – review & editing. **Hongjian Yan:** Methodology, Software. **Jiagang Wu:** Conceptualization, Formal analysis, Resources, Writing – review & editing, Supervision.

#### Declaration of Competing Interest

The authors declare that they have no known competing financial interests or personal relationships that could have appeared to influence the work reported in this paper.

#### Acknowledgments

This work is supported by the National Natural Science Foundation of China (NSFC Nos. 52061130216, 52032007, and 52002252), the Central Funds Guiding the Local Science and Technology Development of Sichuan Province (2021ZYD0022), and the Fundamental Research Fund for the Central Universities (YJ2021154). We appreciate the support from Ms. Hui Wang (Analytical & Testing Center of Sichuan University) for conducting the FE-SEM measurements, and Dr. Bo Gao from the Analytical & Testing Center of Sichuan University for help the LC-MS characterization.

#### Appendix A. Supporting information

Supplementary data associated with this article can be found in the online version at doi:10.1016/j.apcatb.2022.121471.

#### References

- [1] M. Wang, Y. Zuo, J. Wang, Y. Wang, X. Shen, B. Qiu, L. Cai, F. Zhou, S.P. Lau, Y. Chai, Remarkably enhanced hydrogen generation of organolead halide perovskites via piezocatalysis and photocatalysis, *Adv. Energy Mater.* 9 (2019).
- [2] M. Wang, B. Wang, F. Huang, Z. Lin, Enabling PIEZOpotential in PIEZOelectric semiconductors for enhanced catalytic activities, *Angew. Chem. Int. Ed. Engl.* 58 (2019) 7526–7536.
- [3] S. Tu, Y. Guo, Y. Zhang, C. Hu, T. Zhang, T. Ma, H. Huang, Piezocatalysis and piezo-photocatalysis: catalysts classification and modification strategy, reaction mechanism, and practical application, *Adv. Funct. Mater.* 30 (2020).
- [4] Z. Liang, C.-F. Yan, S. Rtimi, J. Bandara, Piezoelectric materials for catalytic/photocatalytic removal of pollutants: recent advances and outlook, *Appl. Catal. B-Eviron.* 241 (2019) 256–269.
- [5] J. Rödel, K.G. Webber, R. Dittmer, W. Jo, M. Kimura, D. Damjanovic, Transferring lead-free piezoelectric ceramics into application, *J. Eur. Ceram. Soc.* 35 (2015) 1659–1681.
- [6] S. Zhang, B. Malić, J.-F. Li, J. Rödel, Lead-free ferroelectric materials: prospective applications, *J. Mater. Res.* 36 (2021) 985–995.
- [7] H.-C. Thong, C. Zhao, Z. Zhou, C.-F. Wu, Y.-X. Liu, Z.-Z. Du, J.-F. Li, W. Gong, K. Wang, Technology transfer of lead-free (K, Na)NbO<sub>3</sub>-based piezoelectric ceramics, *Mater. Today* 29 (2019) 37–48.
- [8] J. Wu, D. Xiao, J. Zhu, Potassium-sodium niobate lead-free piezoelectric materials: past, present, and future of phase boundaries, *Chem. Rev.* 115 (2015) 2559–2595.
- [9] X. Lv, J. Zhu, D. Xiao, X.X. Zhang, J. Wu, Emerging new phase boundary in potassium sodium-niobate based ceramics, *Chem. Soc. Rev.* 49 (2020) 671–707.
- [10] L.Q. Cheng, K. Wang, J.F. Li, One dimensional lead-free (K,Na)NbO<sub>3</sub> nanostructures for a flexible self-powered sensor, *Dalton Trans* 48 (2019) 3984–3989.
- [11] M. Wu, T. Zheng, H. Zheng, J. Li, W. Wang, M. Zhu, F. Li, G. Yue, Y. Gu, J. Wu, High-performance piezoelectric-energy-harvester and self-powered mechanosensing using lead-free potassium-sodium niobate flexible piezoelectric composites, *J. Mater. Chem. A* 6 (2018) 16439–16449.
- [12] L. Jiang, Y. Yang, R. Chen, G. Lu, R. Li, D. Li, M.S. Humayun, K.K. Shung, J. Zhu, Y. Chen, Q. Zhou, Flexible piezoelectric ultrasonic energy harvester array for bio-implantable wireless generator, *Nano Energy* 56 (2019) 216–224.
- [13] Z. Wang, A. Berbille, Y. Feng, S. Li, L. Zhu, W. Tang, Z.L. Wang, Contact-electrocatalysis for the degradation of organic pollutants using pristine dielectric powders, *Nat Commun* 13 (2022) 130.
- [14] J. Yoon, J. Kim, F. Tieves, W. Zhang, M. Alcalde, F. Hollmann, C.B. Park, Piezobiocatalysis: ultrasound-driven enzymatic oxyfunctionalization of C–H Bonds, *ACS Catal.* 10 (2020) 5236–5242.
- [15] R. Su, H.A. Hsain, M. Wu, D. Zhang, X. Hu, Z. Wang, X. Wang, F.T. Li, X. Chen, L. Zhu, Y. Yang, Y. Yang, X. Lou, S.J. Pennycuik, Nano-ferroelectric for high efficiency overall water splitting under ultrasonic vibration, *Angew. Chem. Int. Ed. Engl.* 58 (2019) 15076–15081.
- [16] D. Xia, Z. Tang, Y. Wang, R. Yin, H. He, X. Xie, J. Sun, C. He, P.K. Wong, G. Zhang, Piezo-catalytic persulfate activation system for water advanced disinfection: Process efficiency and inactivation mechanisms, *Chem. Eng. J.* 400 (2020).
- [17] Y. Pang, J.W. Lee, K. Kubota, H. Ito, Solid-state radical C-H trifluoromethylation reactions using ball milling and piezoelectric, *Materials*, *Angew. Chem. Int. Ed. Engl.* 59 (2020) 22570–22576.
- [18] J.M. Wu, W.E. Chang, Y.T. Chang, C.K. Chang, Piezo-catalytic effect on the enhancement of the ultra-high degradation activity in the dark by single- and few-layers MoS<sub>2</sub> nanoflowers, *Adv. Mater.* 28 (2016) 3718–3725.
- [19] P. Zhu, Y. Chen, J. Shi, Piezocatalytic tumor therapy by ultrasound-triggered and BaTiO<sub>3</sub>-mediated piezoelectricity, *Adv. Mater.* 32 (2020), e2001976.
- [20] C. Li, Y. Li, T. Yao, L. Zhou, C. Xiao, Z. Wang, J. Zhai, J. Xing, J. Chen, G. Tan, Y. Zhou, S. Qi, P. Yu, C. Ning, Wireless electrochemotherapy by selenium-doped piezoelectric biomaterials to enhance cancer cell apoptosis, *ACS Appl. Mater. Inter.* 12 (2020) 34505–34513.
- [21] Y. Wang, X. Wen, Y. Jia, M. Huang, F. Wang, X. Zhang, Y. Bai, G. Yuan, Y. Wang, Piezo-catalysis for nondestructive tooth whitening, *Nat Commun* 11 (2020) 1328.
- [22] G. Tan, S. Wang, Y. Zhu, L. Zhou, P. Yu, X. Wang, T. He, J. Chen, C. Mao, C. Ning, Surface-selective preferential production of reactive oxygen species on piezoelectric ceramics for bacterial killing, *ACS Appl. Mater. Inter.* 8 (2016) 24306–24309.
- [23] X. Xu, Y. Jia, L. Xiao, Z. Wu, Strong vibration-catalysis of ZnO nanorods for dye wastewater decolorization via piezo-electro-chemical coupling, *Chemosphere* 193 (2018) 1143–1148.
- [24] W. Feng, J. Yuan, F. Gao, B. Weng, W. Hu, Y. Lei, X. Huang, L. Yang, J. Shen, D. Xu, X. Zhang, P. Liu, S. Zhang, Piezopotential-driven simulated electrocatalytic nanosystem of ultrasmall MoC quantum dots encapsulated in ultrathin N-doped graphene vesicles for superhigh H<sub>2</sub> production from pure water, *Nano Energy* 75 (2020).
- [25] Y. Bai, J. Zhao, Z. Lv, K. Lu, Enhanced piezocatalytic performance of ZnO nanosheet microspheres by enriching the surface oxygen vacancies, *J. Mater. Sci.* 55 (2020) 14112–14124.

- [26] Z. Kang, K. Ke, E. Lin, N. Qin, J. Wu, R. Huang, D. Bao, Piezoelectric polarization modulated novel Bi<sub>2</sub>WO<sub>6</sub>/g-C<sub>3</sub>N<sub>4</sub>/ZnO Z-scheme heterojunctions with g-C<sub>3</sub>N<sub>4</sub> intermediate layer for efficient piezo-photocatalytic decomposition of harmful organic pollutants, *J. Colloid Inter. Sci.* 607 (2022) 1589–1602.
- [27] A. Zhang, Z. Liu, B. Xie, J. Lu, K. Guo, S. Ke, L. Shu, H. Fan, Vibration catalysis of eco-friendly Na<sub>0.5</sub>K<sub>0.5</sub>NbO<sub>3</sub>-based piezoelectric: An efficient phase boundary catalyst, *Appl. Catal. B-Environ.* 279 (2020).
- [28] M. Zhu, S. Li, H. Zhang, J. Gao, K.W. Kwok, Y. Jia, L.-B. Kong, W. Zhou, B. Peng, Diffused phase transition boosted dye degradation with Ba (ZrxTi1-x)O<sub>3</sub> solid solutions through piezoelectric effect, *Nano Energy* 89 (2021).
- [29] Y. Feng, L. Ling, Y. Wang, Z. Xu, F. Cao, H. Li, Z. Bian, Engineering spherical lead zirconate titanate to explore the essence of piezo-catalysis, *Nano Energy* 40 (2017) 481–486.
- [30] P. Wang, X. Li, S. Fan, X. Chen, M. Qin, D. Long, M.O. Tade, S. Liu, Impact of oxygen vacancy occupancy on piezo-catalytic activity of BaTiO<sub>3</sub> nanobelt, *Appl. Catal. B-Environ.* 279 (2020).
- [31] D. Liu, Y. Song, Z. Xin, G. Liu, C. Jin, F. Shan, High-piezocatalytic performance of eco-friendly (Bi<sub>1/2</sub>Na<sub>1/2</sub>)TiO<sub>3</sub>-based nanofibers by electrospinning, *Nano Energy* 65 (2019).
- [32] V.V. Shvartsman, D.C. Lupascu, D.J. Green, Lead-Free Relaxor Ferroelectrics, *J. Am. Ceram. Soc.* 95 (2012) 1–26.
- [33] F. Li, M.J. Cabral, B. Xu, Z. Cheng, E.C. Dickey, J.M. LeBeau, J. Wang, J. Luo, S. Taylor, W. Hackenberger, L. Bellaiche, Z. Xu, L.Q. Chen, T.R. Shrout, S. Zhang, Giant piezoelectricity of Sm-doped Pb(Mg<sub>1/3</sub>Nb<sub>2/3</sub>)O<sub>3</sub>-PbTiO<sub>3</sub> single crystals, *Science* 364 (2019) 264–268.
- [34] M.-H. Zhang, Q. Zhang, T.-T. Yu, G. Li, H.-C. Thong, L.-Y. Peng, L. Liu, J. Ma, Y. Shen, Z. Shen, J. Daniels, L. Gu, B. Han, L.-Q. Chen, J.-F. Li, F. Li, K. Wang, Enhanced electric-field-induced strains in (K,Na)NbO<sub>3</sub> piezoelectrics from heterogeneous structures, *Mater. Today* 46 (2021) 44–53.
- [35] A. Zhang, Z. Liu, X. Geng, W. Song, J. Lu, B. Xie, S. Ke, L. Shu, Ultrasonic vibration driven piezocatalytic activity of lead-free K<sub>0.5</sub>Na<sub>0.5</sub>NbO<sub>3</sub> materials, *Ceram. Int.* 45 (2019) 22486–22492.
- [36] F. Li, D. Lin, Z. Chen, Z. Cheng, J. Wang, C. Li, Z. Xu, Q. Huang, X. Liao, L.Q. Chen, T.R. Shrout, S. Zhang, Ultrahigh piezoelectricity in ferroelectric ceramics by design, *Nat Mater* 17 (2018) 349–354.
- [37] F. Li, L. Jin, Z. Xu, S. Zhang, Electrostrictive effect in ferroelectrics: an alternative approach to improve piezoelectricity, *Appl. Phys. Rev.* 1 (2014).
- [38] X.-x. Sun, J. Zhang, X. Lv, X.-x. Zhang, Y. Liu, F. Li, J. Wu, Understanding the piezoelectricity of high-performance potassium sodium niobate ceramics from diffused multi-phase coexistence and domain feature, *J. Mater. Chem. A* 7 (2019) 16803–16811.
- [39] J. Gao, D. Xue, Y. Wang, D. Wang, L. Zhang, H. Wu, S. Guo, H. Bao, C. Zhou, W. Liu, S. Hou, G. Xiao, X. Ren, Microstructure basis for strong piezoelectricity in Pb-free Ba(Zr<sub>0.2</sub>Ti<sub>0.8</sub>)O<sub>3</sub>-(Ba<sub>0.7</sub>Ca<sub>0.3</sub>)TiO<sub>3</sub> ceramics, *Appl. Phys. Lett.* 99 (2011).
- [40] F. Li, S. Zhang, T. Yang, Z. Xu, N. Zhang, G. Liu, J. Wang, J. Wang, Z. Cheng, Z. G. Ye, J. Luo, T.R. Shrout, L.Q. Chen, The origin of ultrahigh piezoelectricity in relaxor-ferroelectric solid solution crystals, *Nat Commun* 7 (2016) 13807.
- [41] X.-x. Sun, R. Li, C. Zhao, X. Lv, J. Wu, One simple approach, two remarkable enhancements: manipulating defect dipoles and local stress of (K, Na)NbO<sub>3</sub>-based ceramics, *Acta Mater.* 221 (2021).
- [42] T. Zheng, J. Wu, X. Cheng, X. Wang, B. Zhang, D. Xiao, J. Zhu, X. Wang, X. Lou, High strain in (K<sub>0.4</sub>Na<sub>0.6</sub>)(Nb<sub>0.95</sub>Sb<sub>0.05</sub>)O<sub>3</sub>-Bi<sub>0.5</sub>Na<sub>0.5</sub>ZrO<sub>3</sub> lead-free ceramics with large piezoelectricity, *J. Mater. Chem. C* 2 (2014) 8796–8803.
- [43] H. Liu, P. Veber, J. Koruza, D. Rytz, M. Josse, J. Rödel, M. Maglione, Influence of Ta<sup>5+</sup> content on the crystallographic structure and electrical properties of [001] PC-oriented (Li,Na,K)(Nb,Ta)O<sub>3</sub> single crystals, *CrystEngComm* 18 (2016) 2081–2088.
- [44] F.-Z. Yao, K. Wang, W. Jo, K.G. Webber, T.P. Comyn, J.-X. Ding, B. Xu, L.-Q. Cheng, M.-P. Zheng, Y.-D. Hou, J.-F. Li, Diffused phase transition boosts thermal stability of high-performance lead-free piezoelectrics, *Adv. Funct. Mater.* 26 (2016) 1217–1224.
- [45] X.-x. Sun, C. Zhao, X. Lv, J. Wu, Decoding the role of diffused multiphase coexistence in potassium sodium niobate-based ceramics with nanodomains for enhanced piezoelectric devices, *ACS Appl. Nano Mater.* 3 (2019) 953–961.
- [46] J.E. Garcia, F. Rubio-Marcos, Polymorphic phase boundary in piezoelectric oxides, *J. Appl. Phys.* 127 (2020).
- [47] R. Li, B. Tan, T. Zheng, J. Wu, Defect-driven conductivity behavior in lead-free KNN-based ceramics, *J. Appl. Phys.* 127 (2020).
- [48] Y.-X. Liu, H.-C. Thong, C. Zhao, Q. Liu, X. Xu, K. Wang, J.-F. Li, Influence of trace zirconia addition on the properties of (K,Na)NbO<sub>3</sub> solid solutions, *J. Mater. Chem. C* 7 (2019) 6914–6923.
- [49] W. Yang, P. Li, S. Wu, F. Li, B. Shen, J. Zhai, A study on the relationship between grain size and electrical properties in (K,Na)NbO<sub>3</sub>-based lead-free piezoelectric ceramics, *Advanced Electronic Materials* 5 (2019).
- [50] P. Li, J. Zhai, B. Shen, S. Zhang, X. Li, F. Zhu, X. Zhang, Ultrahigh piezoelectric properties in textured (K,Na)NbO<sub>3</sub>-based lead-free ceramics, *Adv. Mater.* 30 (2018).
- [51] X. Lv, N. Zhang, J. Wu, X.-x. Zhang, The role of adding Bi<sub>0.5</sub>A<sub>0.5</sub>ZrO<sub>3</sub> in affecting orthorhombic-tetragonal phase transition temperature and electrical properties in potassium sodium niobate ceramics, *Acta Mater* 197 (2020) 224–234.
- [52] F. Mushtaq, X. Chen, M. Hoop, H. Torlakcik, E. Pellicer, J. Sort, C. Gattinoni, B. J. Nelson, S. Pane, Piezoelectrically enhanced photocatalysis with BiFeO<sub>3</sub> nanostructures for efficient water remediation, *iScience* 4 (2018) 236–246.
- [53] P.-C. Li, C.-Y. Tang, L. Cheng, Y.-M. Hu, X.-H. Xiao, W.-P. Chen, Reduction of CO<sub>2</sub> by TiO<sub>2</sub> nanoparticles through friction in water, *Acta Physica Sinica* 70 (2021).
- [54] P. Li, C. Tang, X. Xiao, Y. Jia, W. Chen, Flammable gases produced by TiO<sub>2</sub> nanoparticles under magnetic stirring in water, *Friction* (2021).
- [55] R.T. Poole, D.R. Williams, J.D. Riley, J.G. Jenkin, J. Liesegang, R.C.G. Leckey, Electronegativity as a unifying concept in the determination of Fermi energies and photoelectric thresholds, *Chem. Phys. Lett* 36 (1975) 401–403.
- [56] C. Wu, H. Yan, J. Zhong, J. Xie, D. Wang, Y. Shi, L. Zhang, J. Zhu, Q. Chen, Tape casting and phase inversion derived easily recyclable PVDF@g-C<sub>3</sub>N<sub>4</sub>/Bi<sub>2</sub>WO<sub>6</sub> porous film for high performance and long-term photocatalytic pollutants degradation, *Appl. Surf. Sci.* 496 (2019).
- [57] E. Lin, J. Wu, N. Qin, B. Yuan, Z. Kang, D. Bao, Enhanced piezocatalytic, photocatalytic and piezo-/photocatalytic performance of diphasic Ba<sub>1-x</sub>CaxTiO<sub>3</sub> nanowires near a solubility limit, *Catalysis Science & Technology* 9 (2019) 6863–6874.
- [58] X. Zhou, S. Wu, C. Li, F. Yan, H. Bai, B. Shen, H. Zeng, J. Zhai, Piezophototronic effect in enhancing charge carrier separation and transfer in ZnO/BaTiO<sub>3</sub> heterostructures for high-efficiency catalytic oxidation, *Nano Energy* 66 (2019).
- [59] C. Yu, S. Lan, S. Cheng, L. Zeng, M. Zhu, Ba substituted SrTiO<sub>3</sub> induced lattice deformation for enhanced piezocatalytic removal of carbamazepine from water, *J. Hazard. Mater.* 424 (2022).
- [60] X. Zhou, Q. Sun, D. Zhai, G. Xue, H. Luo, D. Zhang, Excellent catalytic performance of molten-salt-synthesized Bi<sub>0.5</sub>Na<sub>0.5</sub>TiO<sub>3</sub> nanorods by the piezo-phototronic coupling effect, *Nano Energy* 84 (2021).